



Total oxidation of volatile organic compounds on Au/FeO_x catalysts supported on mesoporous SBA-15 silica

R. Bonelli^{a,b}, C. Lucarelli^{a,b,c}, T. Pasini^{a,b}, L.F. Liotta^d, S. Zacchini^e, S. Albonetti^{a,b,*}

^a Dip. Chimica industriale e dei Materiali, Viale Risorgimento 4, 40136 Bologna, Italy

^b INSTM, Research Unit of Bologna, Italy

^c Dip. Scienze Chimiche e Ambientali, Via Valleggio 11, 22100 Como (CO), Italy

^d Istituto per Lo Studio dei Materiali Nanostrutturati (ISMN)-CNR, Via Ugo La Malfa 153, 90146 Palermo, Italy

^e Dip. Chimica Fisica ed Inorganica, Viale Risorgimento 4, 40136 Bologna, Italy

ARTICLE INFO

Article history:

Received 20 January 2011

Received in revised form 8 April 2011

Accepted 11 April 2011

Available online 16 April 2011

Keywords:

Catalytic combustion

Gold/iron catalysts

Cluster-derived catalysts

ABSTRACT

A series of Au/FeO_x/SBA-15 type materials were prepared by two methods: one conventional and one non-conventional: gold deposition-precipitation on FeO_x/SBA-15 and bimetallic carbonyl cluster deposition on SBA-15, respectively.

Both chemical physical characterization and catalytic activity tests in the complete combustion of methanol show that the new preparation method of Au/FeO_x-supported catalysts leads to the anchoring of the Au by modifying the surface of SBA-15 with FeO_x species. This effect results in a considerable improvement in catalyst performance as compared to the classic preparation by deposition-precipitation of Au on SBA-15 and FeO_x/SBA-15.

© 2011 Elsevier B.V. All rights reserved.

1. Introduction

Highly dispersed gold catalysts supported on different solids have shown high catalytic activity toward many reactions of industrial and environmental significance [1]. A sizable number of applications have been found for the selective oxidation of several compounds [2–4] and the role of gold in the total oxidation of different types of saturated and unsaturated hydrocarbons, unsaturated carbonyl compounds, alkynes, and alkadienes – the so-called volatile organic compounds (VOCs) – has also been extensively studied [5]. The removal of VOCs has received particular attention due to the fact that they have been associated with: (i) the increase in photochemical smog in urban environments, (ii) the depletion of atmospheric ozone, and (iii) the production of ground-level ozone [6,7]. Gold supported on different oxides such as Al₂O₃ and MO_x-doped Al₂O₃ (M: Ce, Mn, Co, Fe, Mo), TiO₂, Fe₂O₃, and CeO₂ [8–21] has shown high activities for the catalytic oxidation of different kinds of VOCs. The electronic state of gold species and the size of gold particles determine the activity toward the catalytic combustion of VOCs of such systems. Moreover, gold nanoparticles supported over reducible oxides increase the mobility of the lattice oxygen involved in the reaction mechanism.

Since the discovery of ordered mesoporous silica materials in the 1990s, synthesis and applications of mesoporous solids have been studied extensively [22]. When silica is used as a support it is very difficult to obtain an optimal gold dispersion due to the low affinity of gold for such an inert support [23]. Mesoporous SBA-15 – with a highly ordered 2D hexagonal structure, well-defined pore size, and thicker walls – seems to be an ideal candidate for obtaining a strong confinement of gold nanoparticles. To increase the metal dispersion on this support, the functionalization of its surface either by molecules such as organo-silane [24,25] or by different oxides such as TiO₂, CeO₂, Co₃O₄ [26–28] is necessary.

The greatest advantages of the surface functionalization by an active oxide layer are the stabilization of the highly dispersed gold deposited on SBA-15, and the strong interaction between gold and oxides, which leads to an increased catalytic activity.

In literature the beneficial effect of the addition of iron to gold-supported catalysts, in terms of enhanced activity, selectivity, resistance to deactivation, and prolonged lifetime of the catalyst has been extensively demonstrated [10,29–34]. FeO_x species were found to act as a structural promoter but also as a co-catalyst: it was proved that gold particles are stabilized against sintering while the lattice oxygen of the oxide plays an active role via the Mars-van Krevelen mechanism.

In our previous works [35–37] we demonstrated that it is possible to synthesize titania- and ceria-supported catalysts containing FeO_x-stabilized gold nanoparticles with a controlled size and an intimate contact between gold and iron oxide species by using bi-metallic carbonyl clusters as precursors of the active phase.

* Corresponding author at: Dip. Chimica industriale e dei Materiali, Viale Risorgimento 4, 40136 Bologna, Italy. Tel.: +39 051 2093681; fax: +39 051 2093680.

E-mail address: stefania.albonetti@unibo.it (S. Albonetti).

Thus, in the present work, we investigated the possibility of obtaining small gold nanocrystallites, anchored to mesoporous SBA-15 via an iron layer by using the above-mentioned method previously developed by us, which uses the bi-metallic carbonyl cluster salt $[\text{NEt}_4][\text{AuFe}_4(\text{CO})_{16}]$ as precursor of gold and iron oxides species. Prepared catalysts were tested in the total oxidation of methanol, used as probe molecule of oxygenated VOC.

2. Experimental

2.1. Catalyst preparation

Mesoporous SBA-15 was prepared starting from tetraethyl orthosilicate (TEOS, Aldrich 98%), as silica source and using a triblock poly(ethylene oxide)–poly(propylene oxide)–poly(ethylene oxide) (EO20PO70EO20, Pluronic P123, Aldrich), as template, according to the published procedure [38]. In a typical preparation, 8.1 g Pluronic P123 was dissolved in 146.8 g de-ionized water and 4.4 g of conc. HCl (37%) and stirred overnight at 35 °C in a 250 ml single-neck flask. To this solution, 16 g of TEOS was quickly added and stirred for 24 h at 35 °C. The milky suspension was annealed at 100 °C for 24 h in a closed polypropylene bottle. The solid product was filtered, washed with an HCl/water-mixture and calcined at 550 °C for 5 h in air.

One FeO_x and one Au/FeO_x sample, containing respectively Fe 2.3 wt.% and Au 2 wt.% + Fe 2.3 wt.%, were prepared by impregnation of the monometallic $[\text{NEt}_4][\text{HFe}_3(\text{CO})_{11}]$ [39] and bimetallic $[\text{NEt}_4][\text{AuFe}_4(\text{CO})_{16}]$ [40] carbonyl cluster salts on the prepared mesoporous silica. In a typical experiment, the required amount of the carbonyl cluster was dissolved in degassed acetone (20–40 ml) under nitrogen and added dropwise over a period of 1 h to an acetone suspension of SBA-15 (5 g), which was previously degassed and stored under nitrogen. The resulting suspension was allowed to stir overnight, then the solvent was removed in vacuum at room temperature; lastly, the prepared samples were stored in air at ambient temperature and dried at 100 °C for 2 h in air.

For comparison, one Au- and one Au/FeO_x -containing catalyst were prepared by introducing 2 wt.% of Au by the deposition-precipitation (DP) method, using the HAuCl_4 precursor and urea, on bare SBA-15 and on the previously prepared FeO_x sample. These systems were filtered, washed thoroughly, and dried at 100 °C overnight. All catalysts were treated at 400 °C for 2 h (by heating from room temperature at a rate of 10 °C/min) in flowing N_2 in order to control the Au crystal growth.

Prepared samples will be denoted by the abbreviation “Fe” and “FeAu” combined with the letters “C” and “DP”, which indicate the different preparation methods: C is cluster deposition while DP refers to the deposition-precipitation method. Samples indicated as “spent” or “used” refer to catalysts tested in the reaction up to 350 °C for a run of 60 h. Code and composition of prepared catalysts are shown in Table 1.

2.2. Characterization of the catalysts

Surface area measurements (BET) [41] and pore size distribution (BJH) [42] were carried out by means of a Micromeritics ASAP 2020 instrument. The samples were previously outgassed at 150 °C until a $P = 0.04$ bar was reached, then kept for 30 min at this temperature, and lastly heated up to 250 °C and maintained at that temperature for 30 min.

The real metal content on catalysts was determined by ICP-AES analysis with a Fision 3410+ instrument.

Small-angle X-ray scattering (SAXS) experiments were performed on a Bruker Nanostar SAXS System equipped with 2D detector using Cu $K\alpha$ radiation ($\lambda = 1.5418 \text{ \AA}$). The SAXS measure-

ments were collected in the range of 0.2–4.7° 2θ by using a 0.02° step size and a counting time of 1.3 s per step.

Wide-angle X-ray diffraction (XRD) measurements were carried out at room temperature with a Bragg/Brentano diffractometer (X'pertPro Panalytical) equipped with a fast X'Celerator detector, using Cu anode as X-ray source ($K\alpha$, $\lambda = 1.5418 \text{ \AA}$). For all samples the complete diffractogram was collected in the range of 10–85° in 2θ by using a 0.05° step size and a counting time of 20 s per step. For the Au crystal size evaluation, a second acquisition was made in the range of 36–42° in 2θ by using a longer counting time, i.e. 400 s per step, and a step size of 0.03°. The coherent length of the Au crystalline domains was evaluated through single line profile fitting of the reflection at 38.2° 2θ , by calculating Au crystal size values from the widths at half maximum intensity by the Scherrer equation [43]. The assignment of the various crystalline phases was based on the JCPDS powder diffraction file cards [44].

Diffuse reflectance UV–vis (DR-UV-Vis) spectra were recorded in the range of 200–800 nm with a UV/VIS/NIR Perkin Elmer spectrometer Lambda 19.

The reduction behavior of different samples was studied by means of temperature programmed reduction using a Thermoquest TPDRO instrument under 5 vol.% H_2/Ar flow (20 ml min⁻¹). The temperature was raised from 60 to 700 °C by a heating rate of 10 °C min⁻¹.

Catalytic experiments with methanol were performed in a continuous-flow fixed-bed microreactor. Each test was carried out by loading 0.13 g of catalyst (30–60 mesh) diluted with an inert glass powder. The total volumetric flow through the catalyst bed was held constant at 140 ml min⁻¹, 10 vol.% oxygen, 90 vol.% nitrogen and 2600 ppm of methanol. Analyses of reactants and products were carried out as follows: the products in the outlet stream were scrubbed in cold isopropanol maintained at –20 °C by a F32 Julabo Thermostat. Analyses of reactants and products were carried out with a GC Clarus 500 (Perkin Elmer) equipped with a capillary column Elite FFAP (30 m × 0.32 mm) and a capillary column Elite Plot Q (30 m × 0.32 mm) attached to a methanizer assembly flame ionization detector (FID). CO_2 and water were the main products detected for $\text{Au/FeO}_x/\text{SBA-15}$ catalysts. At low methanol conversion (<20%), some CO and methyl formate, as intermediate products, were observed.

3. Results and discussion

3.1. Textural properties of support and catalysts

Small-angle X-ray scattering was carried out to study the ordered porous structure of SBA-15 and the supported catalysts. N_2 -adsorption/desorption measurements were performed to get insight the textural properties of the materials. The SAXS patterns, shown in Fig. 1, displayed three well-resolved peaks at 0.92°, 1.58°, and 1.83° 2θ , respectively, which correspond to (1 0 0), (1 1 0), and (2 0 0) reflections of the hexagonal arrays in the mesoporous structure of SBA-15 [45]. The SAXS patterns of metal catalysts were essentially identical, regardless of the metal and preparation method, showing peaks at the same angular positions, at 0.95°, 1.63°, and 1.89° 2θ . The shift from 0.92 to 0.95° 2θ of the first peak, observed for the metallic carbonyl cluster-derived catalysts, and the decrease in the calculated d_{100} space from 9.6 nm (for pure SBA-15) to 9.3 nm are consistent with previous literature reports [46,47], and suggest that metal deposition occurred inside the pore channels of SBA-15. The decreased intensity of the SBA-15 diffraction peaks detected for the Au/FeO_x catalysts further confirms the progressive coating of the mesopores walls, which depends on both the metal loading and the preparation method. On the other hand, the presence of detectable (1 1 0) and (2 0 0) reflection peaks in the

Table 1
Code and composition of studied catalysts.

Catalyst	Salt precursor	Fe loading (wt.%)		Au loading (wt.%)		Preparation method
		Nominal	Measured ^a	Nominal	Measured ^a	
C-Fe	[NEt ₄][HFe ₃ (CO) ₁₁]	2.3	2.1	–	–	Cluster impregnation
C-FeAu	[NEt ₄][AuFe ₄ (CO) ₁₆]	2.3	2.2	2.0	2.0	Cluster impregnation
C-Fe DP-Au	[NEt ₄][HFe ₃ (CO) ₁₁] + HAuCl ₄	2.3	2.1	2.0	1.9	Cluster impregnation + Au DP method
DP-Au	HAuCl ₄	–	–	2.0	1.9	Au DP method

^a Determined by ICP analysis.

Table 2
Porosity and Au average crystallite size on both fresh and used catalysts for studied Au materials.

Catalyst	Surface area (m ² /g)	Pore diameter (nm)	Pore volume (cm ³ /g)	Au crystallite size – fresh (nm)	Au crystallite size – spent ^a (nm)
SBA-15	760	6.7	0.75	–	–
C-Fe	725	5.0	0.89	–	–
C-FeAu	526	4.6	0.63	<3	5
C-Fe DP-Au	493	4.6	0.69	10	10
DP-Au	353	7.5	0.87	13	16

^a Catalysts tested in the total oxidation of methanol.

catalysts confirms that metal introduction does not destroy the ordered arrangement of the SBA-15 channel package [46]. Surprisingly, when gold was introduced by the conventional DP method, the (100), (110), and (200) reflection peaks of the catalyst are at the same angular position that is typical of bare SBA-15, thus suggesting that in this case the growth of gold clusters occurs preferentially on the surface of the support rather than within the confined mesopore space. However, in comparison with SBA-15, the peak (100) appeared decreased in intensity and broadened, thus indicating that a wider range of pore structures is developed in this catalyst, probably as a consequence of the obstruction of the smallest pores due to the presence of gold. It is likely that gold particles, at first deposited inside the porous structure of SBA-15, during the calcinations treatment – due to the weak interaction with the support – migrate toward the outside of the pores with consequent agglomeration and sintering. Accordingly, the average Au crystallite size (13 nm) (Table 2), calculated by the Scherrer equation on the basis of the catalyst diffraction pattern, exceeded the SBA-15 mesopore diameter.

N₂ adsorption–desorption isotherms data are shown in Fig. 2 and Table 2, respectively. For all samples, the isotherms are identified as type IV according to the IUPAC classification, which is a typical characteristic of mesoporous materials [48], and a clear H1-type hysteresis loop is observed, thus indicating the presence of uniform cylindrical pore channels [49]. A very small decrease in

the specific surface area (see Table 2) and a hysteresis loop similar to the support were observed for C-Fe catalyst, thus indicating that the deposition of the iron carbonyl cluster does not modify the structural properties of the mesoporous SBA-15. On the other hand, it is possible to observe that the hysteresis loops of the bimetallic catalysts become smaller than SBA-15 and the isotherm shifts to lower pressure, whereas the adsorption branch does not change significantly. Thus, in the presence of gold, a partial occlusion of the mesopores is induced on the support surface. This effect was found to be moderate when gold is either introduced at the same time as iron by employing the bi-metallic cluster, or deposited by DP on the C-Fe sample, whereas, in the absence of iron, the SBA-15 surface and structure are more affected by gold nanoparticles. In fact, in the case of the DP-Au sample, in addition to a lower amount of N₂ adsorbed in the low pressure range, a different hysteresis shape was observed, and the relative pressure where the capillary condensation step occurs shifted to higher P/P_0 values. It is likely that during the calcination treatment some gold nanoparticles crystallized inside the smallest pores of SBA-15, thus partially blocking them from the outside. As a consequence, the mean pore size distribution shifted to higher values, as did the pore volume (Table 2). At the same time, gold nanoclusters partially sintered on the external surface of SBA-15.

3.2. Wide-angle X-ray diffraction

The wide-angle XRD patterns collected for all catalysts are shown in Fig. 3. For all samples, a broad peak at $2\theta = 22^\circ$, attributable to the amorphous framework of SBA-15, was observed.

Two weak peaks at $2\theta = 33.2^\circ$ and 35.7° , which were attributable to the most intense reflections of the Fe₂O₃ hematite phase, were detected on C-Fe and C-Fe DP-Au catalysts, while no reflections due to iron and gold species could be observed on C-FeAu, thus indicating the effectiveness of this preparation method in obtaining an optimal metal dispersion on the catalyst surface as well as very small gold nanocrystallites stabilized via an iron layer. On the contrary, intense reflections attributable to metallic gold were detected in the patterns of DP-Au and C-Fe DP-Au. According to the literature [23], the weak metal–support interaction between gold and silica easily lead to particle aggregation and growth. However, the presence of the iron layer in the C-Fe DP-Au sample was conducive to slightly better gold dispersion and stabilization as compared to the iron-free DP-Au, as can be inferred from the average crystallite size of gold indicated in Table 2.

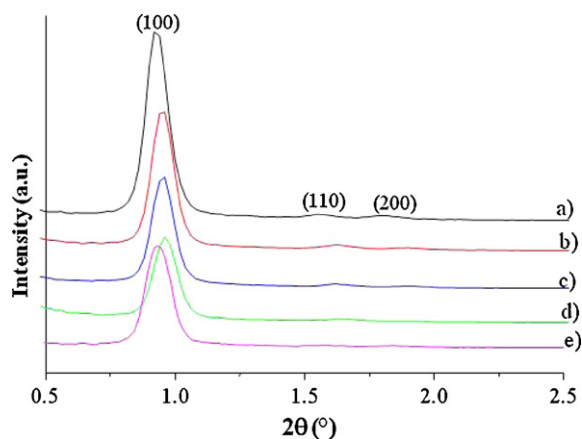


Fig. 1. Small angle X-ray diffraction patterns of (a) SBA-15, (b) C-Fe, (c) C-FeAu, (d) C-Fe DP-Au and (e) DP-Au.

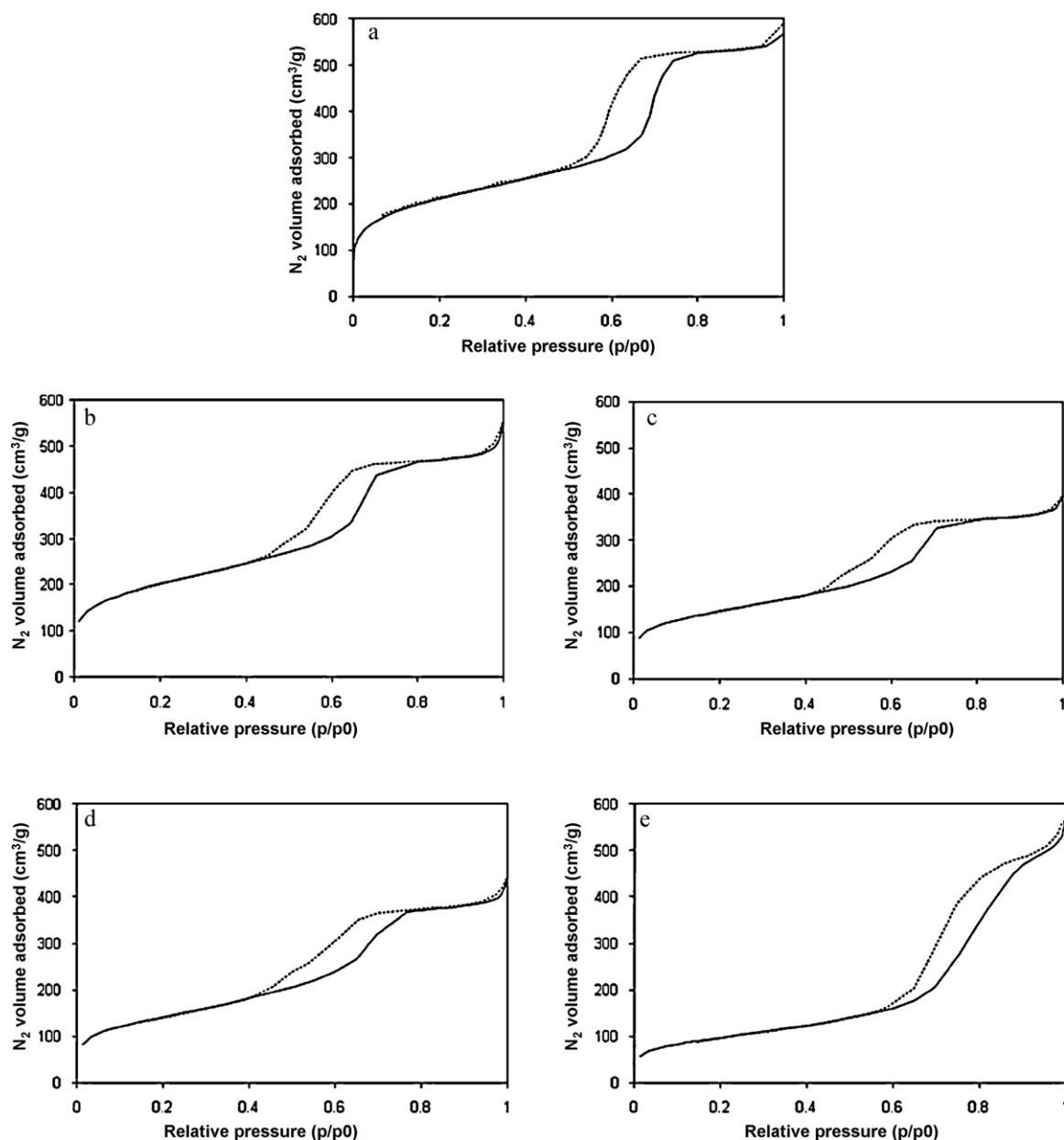


Fig. 2. Nitrogen adsorption (full line) and desorption (dotted line) of (a) SBA-15, (b) C-Fe, (c) C-FeAu, (d) C-Fe DP-Au and (e) DP-Au.

3.3. UV–vis diffuse reflectance spectra

In order to study the iron and gold structure of SBA-15 supported catalysts, UV–vis diffuse reflectance measurements were performed.

Fig. 4 shows diffuse reflectance UV–vis spectra. Au/FeO_x samples exhibit both typical absorption bands at wavelength below 400 nm, which correspond to different iron species [50], and the plasmon band in the range of 500–600 nm due to the presence of gold nanoparticles [51,52]. For the C-Fe sample, two different absorption bands at 215 and 260 nm were observed, thus indicating the presence of isolated Fe³⁺ monomer sites which generally show bands below 300 nm [53,54]. An increased absorption above 300 nm was observed for both C-FeAu and C-Fe DP-Au catalysts attributed to Fe³⁺ in small oligomeric Fe_mO_n species. At longer wavelengths, above 400 nm, an overlapping of the typical plasmon resonance peak of metallic gold, around 525 nm, and bands originated from Fe₂O₃ hematite nanoparticles is likely to occur

[53,54]. According to the XRD pattern (see Fig. 3), it is reasonable that features of crystalline Fe₂O₃ are present in the spectrum of C-Fe DP-Au. For the monometallic DP-Au catalyst, only the intense band at 525 nm was detected. A sharper peak in DR-UV–vis spectra should imply larger Au particles [55,10]. Likewise, the bandwidth increased from DP-Au to C-Fe DP-Au, with crystallite size decreasing from 13 to 10 nm. Moreover, the peak position and full width of the plasmon band is reported to depend on the shape and surrounding environment of gold [56]. Accordingly, the broadening and red shift of the plasmon band from 525 nm for DP-Au to 540 nm for C-FeAu would be attributed to a different environment surrounding Au nanocrystallites, likely due to a strong interaction with iron oxide species.

3.4. H₂-TPR

Temperature-programmed reduction (TPR) profiles of prepared samples are given in Fig. 5. In the profile of C-Fe two reduction peaks

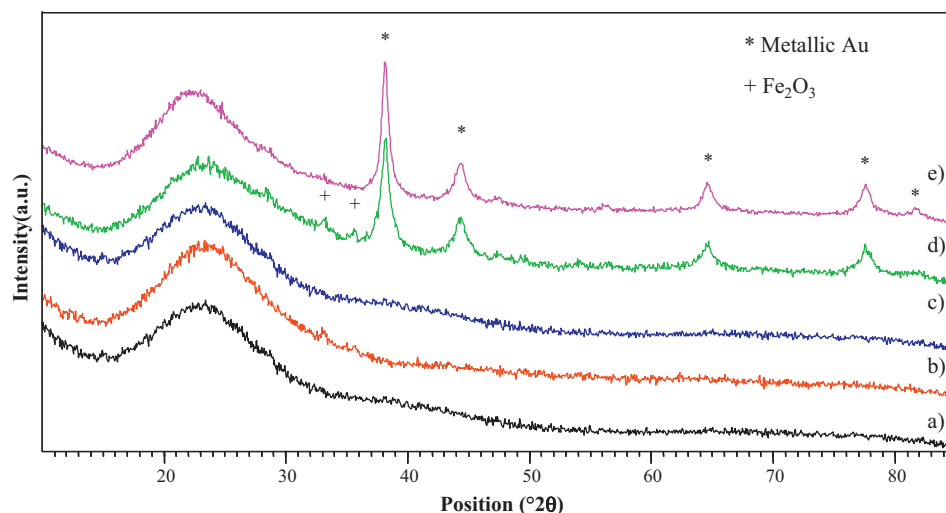


Fig. 3. Wide angle X-ray diffraction patterns of (a) SBA-15, (b) C-Fe, (c) C-FeAu, (d) C-Fe DP-Au and (e) DP-Au.

were present, at 395 °C and around 480 °C. According to previous results [13,57–59], these peaks may be attributed to the reduction to Fe₃O₄ magnetite of hydroxylated and nonhydroxylated Fe₂O₃, respectively. Catalysts prepared by using the gold/iron carbonyl cluster contain very high reducible species. In fact, a peak at about 130 °C was observed for the C-FeAu sample, attributed to the reduction of hydroxylated Fe₂O₃ species strongly interacting with gold, thus confirming that the presence of gold strongly facilitates the reduction of Fe₂O₃ species [56,58,59]. This effect was not observed during the reduction process of C-Fe DP-Au, the profile of which was found to be very similar to C-Fe and even shifted to a slightly higher temperature. This behavior indicates that low interaction between gold and iron oxide species was achieved by separately depositing the two metal species, while the shift of TPR peaks to a higher reduction temperature could be due to the presence of the crystalline Fe₂O₃ identified by XRD.

Silica is traditionally regarded as an inert and non-reducible oxide. Accordingly, no hydrogen consumption was observed for

SBA-15 oxide. Conversely, a reduction peak centered at 567 °C was detected for DP-Au, while no reduction peak for gold was observed at low temperature, hence confirming that it is in metallic state. Recently, it has been reported that, in the case of Au nanoparticles confined in aluminosilicate (i.e. Al-SBA-15), it is possible to produce electron-rich defects, only after a severe hydrogen reduction process at 600 °C [60,61]. In such process the oxygen atom in Si–O–Si bonds may be abstracted by hydrogen to produce the defects. This would produce hydrogen consumption at around 600 °C, as experimentally observed in the reduction profile of the DP-Au catalyst.

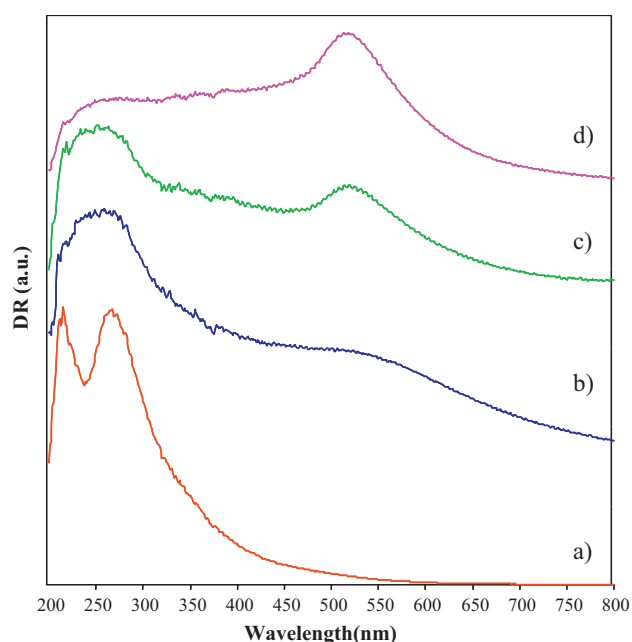


Fig. 4. UV-vis spectra of (a) C-Fe, (b) C-FeAu, (c) C-Fe DP-Au and (d) DP-Au.

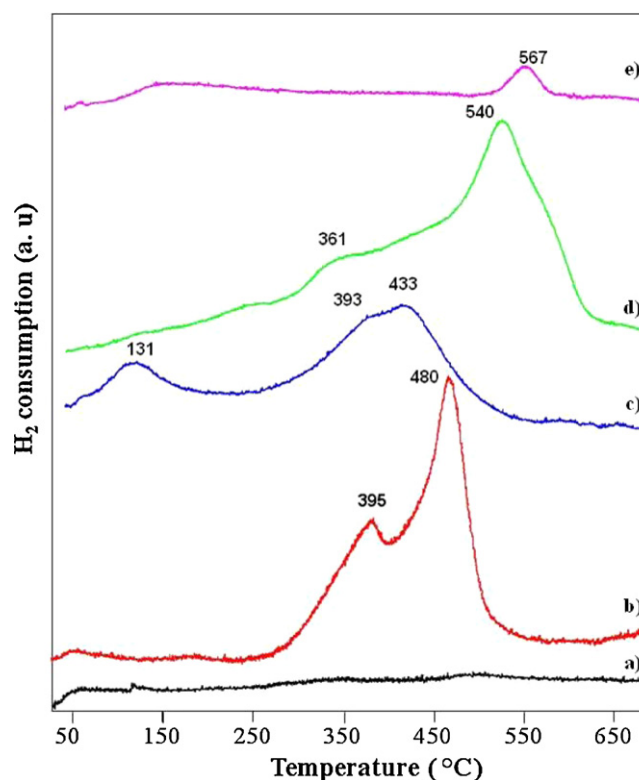


Fig. 5. H₂-TPR analysis of (a) SBA-15, (b) C-Fe, (c) C-FeAu, (d) C-Fe DP-Au and (e) DP-Au.

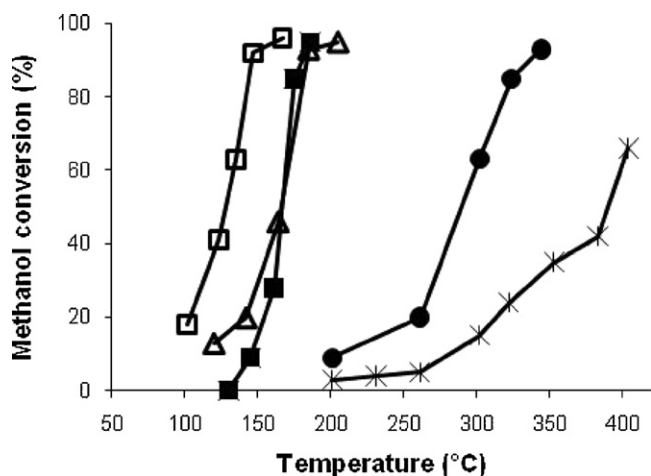


Fig. 6. Methanol conversion as a function of reaction temperature for SBA-15 supported catalysts [Symbols: SBA-15 (X), C-Fe (●), C-FeAu (□), C-Fe DP-Au (Δ) and DP-Au (■)]. Reaction conditions: reactant mixture 0.3 vol.% methanol, 10 vol.% O₂, N₂ balance. Space velocity (GHSV): 7.6×10^{-3} mol_{VOC} h⁻¹ g_{cat}⁻¹.

3.5. Activity measurements

Fig. 6 shows temperature profiles of methanol combustion on prepared catalysts. In all cases CO₂ was the main product detected in the temperature range studied, with selectivity values >90% for Au/FeO_x catalysts. For comparison purposes the activity of bare SBA-15 – which is not very active toward this reaction – has also been indicated. C-Fe was found to be scarcely efficient in the methanol removal, being active only above 200 °C. Gold-containing catalysts showed much higher activity compared to gold-free samples. Very similar light-off curves were obtained for DP-Au and C-Fe DP-Au. The previous deposition of highly dispersed FeO_x species improved Au dispersion on the mesoporous SBA-15 and favored its stabilization under reaction conditions, as can be inferred from the Au crystallite size of the fresh and spent catalysts shown in Table 2; however, the observed catalytic performances confirmed that only a weak interaction is achieved between the two metals when they are separately deposited on SBA-15. The TPR results corroborated this hypothesis, the reduction behavior of C-Fe DP-Au being very similar to C-Fe. Conversely, in the case of the cluster-derived bimetallic catalyst, C-FeAu, a strong synergistic effect was observed between highly dispersed iron oxide and gold nanocrystallites. This sample showed the best performance in methanol deep oxidation. In fact, methanol combustion started below 100 °C and total conversion was achieved at 150 °C. The activity of this catalyst was comparable to the performances of Au supported on bare reducible oxides, e.g. Fe₂O₃ and CeO₂ [12–14,17].

These results, together with TPR and XRD data, confirmed that the simultaneous introduction of the two species by means of a [NET₄][AuFe₄(CO)₁₆] bi-metallic carbonyl cluster, besides anchoring gold nanocrystallites to the surface by an iron oxide layer, leads to a strong interaction between the two species. In this way, in addition to an optimal gold stabilization against sintering during thermal treatment and under reaction conditions, higher iron oxide reducibility is achieved, leading to an improved catalytic activity of these systems.

4. Conclusions

The use of carbonyl clusters is a promising way to obtain iron-stabilized gold nanocrystallites on SBA-15; it could also enable avoiding a further functionalization of the support in order to obtain highly dispersed gold catalysts.

An optimal gold and iron dispersion and a strong interaction between Au and iron oxide species were observed for the bimetallic cluster-derived material. The catalyst prepared by using [NET₄][AuFe₄(CO)₁₆] showed the best performance in terms of methanol combustion, which was induced by the strong synergy occurring between the two metal species originated from a bimetallic precursor with a well-defined molecular structure. The catalytic performance in methanol total oxidation achieved over such catalysts compares very favorably with literature results.

Acknowledgements

We thank the University of Bologna (Project CLUSTERCAT) for funding. The European Community support, through the Network of Excellence IDECAT (Integrated Design of Catalytic Nanomaterials for a Sustainable Production) is also acknowledged.

References

- [1] G.C. Bond, C. Louis, D.T. Thompson, in: G.J. Hutchings (Ed.), *Catalysis by Gold*, vol. 6, Imperial College Press, London, 2006.
- [2] K.M. Parida, N. Sahu, A.K. Tripathi, V.S. Kamble, *Environ. Sci. Technol.* 44 (2010) 4155–4160.
- [3] P. Mohapatra, J. Moma, K.M. Parida, W.A. Jordaan, M.S. Scurrel, *Chem. Commun.* (2007) 1044–1046.
- [4] M. Haruta, *Chem. Rec.* 3 (2003) 75–87.
- [5] M. Haruta, *Catal. Today* 36 (1997) 153–166.
- [6] M. Amann, M. Lutz, *J. Hazard. Mater.* 78 (2000) 41–62.
- [7] R.M. Heck, R.J. Farrauto, *Catalytic Pollution Control*, second ed., Wiley-Interscience, New York, 2002.
- [8] M.A. Centeno, M. Paulis, M. Montes, J.A. Odriozola, *Appl. Catal. A: Gen.* 234 (2002) 65–78.
- [9] M.A. Centeno, M. Paulis, M. Montes, J.A. Odriozola, *Appl. Catal. B: Environ.* 61 (2005) 177–183.
- [10] A.C. Gluhoi, N. Bogdanchikova, B.E. Nieuwenhuys, *J. Catal.* 229 (2005) 154–162.
- [11] L. Delannoy, K. Fajerberg, P. Lakshmanan, C. Potvin, C. Methivier, C. Louis, *Appl. Catal. B: Environ.* 94 (2010) 117–124.
- [12] S. Minicò, S. Scirè, C. Crisafulli, S. Galvagno, *Appl. Catal. B: Environ.* 34 (2001) 277–285.
- [13] S. Minicò, S. Scirè, C. Crisafulli, R. Maggiore, S. Galvagno, *Appl. Catal. B: Environ.* 28 (2000) 245–251.
- [14] S. Scirè, S. Minicò, C. Crisafulli, S. Galvagno, *Catal. Commun.* 2 (2001) 229–232.
- [15] M.L. Jia, H.F. Bai Zhaorigetu, Y.N. Shen, Y.F. Li, *J. Rare Earths* 26 (2008) 528–531.
- [16] B. Solsona, T. Garcia, R. Murillo, A.M. Mastral, E.N. Ndifor, C.E. Hetrick, M.D. Amiridis, S.H. Taylor, *Top. Catal.* 52 (2009) 492–500.
- [17] S. Scirè, S. Minicò, C. Crisafulli, C. Satriano, A. Pistone, *Appl. Catal. B: Environ.* 40 (2003) 43–49.
- [18] D. Andreeva, P. Petrova, J.W. Sobczak, L. Ilieva, M. Abrashev, *Appl. Catal. B: Environ.* 67 (2006) 237–245.
- [19] Y. Shen, X. Yang, Y. Wang, Y. Zhang, H. Zhu, L. Gao, M. Jia, *Appl. Catal. B: Environ.* 79 (2008) 142–148.
- [20] C. Cellier, S. Lambert, E.M. Gaigneaux, C. Poleunis, V. Ruaux, P. Eloy, C. Lahousse, P. Bertrand, J.-P. Pirard, P. Grange, *Appl. Catal. B: Environ.* 70 (2007) 406–416.
- [21] L.F. Liotta, G. Di Carlo, G. Pantaleo, A.M. Venezia, G. Deganello, L. Retailleau, A. Boreave, A. Giroir-Fendler, *Appl. Catal. B: Environ.* 101 (2011) 629–637.
- [22] C.T. Kresge, M.E. Leonowicz, W.J. Roth, J.C. Vartuli, J.S. Beck, *Nature* 359 (1992) 710–712.
- [23] W.T. Wallace, B.K. Min, D.W. Goodman, *J. Mol. Catal. A: Chem.* 228 (2005) 3–10.
- [24] M.G. Cutrufello, E. Rombi, C. Cannas, M. Casu, A. Virga, S. Fiorilli, B. Onida, I. Ferino, *J. Mater. Sci.* 44 (2009) 6644–6653.
- [25] E. Rombi, M.G. Cutrufello, C. Cannas, M. Casu, D. Gazzoli, M. Occhiuzzi, R. Monaci, I. Ferino, *Phys. Chem. Chem. Phys.* 11 (2009) 593–602.
- [26] A. Beck, A. Horváth, G. Stefler, R. Katona, O. Geszti, Gy. Tolnai, L.F. Liotta, L. Guzzi, *Catal. Today* 139 (2008) 180–187.
- [27] A. Beck, A. Horváth, G. Stefler, M.S. Scurrell, L. Guzzi, *Top. Catal.* 52 (2009) 912–919.
- [28] X. Xu, J. Li, Z. Hao, W. Zhao, C. Hu, *Mater. Res. Bull.* 41 (2006) 406–413.
- [29] A.C. Gluhoi, B.E. Nieuwenhuys, *Catal. Today* 119 (2007) 305–310.
- [30] F.W. Chang, H.Y. Yu, L. Selva Roselin, H.C. Yang, T.C. Ou, *Appl. Catal. A: Gen.* 302 (2006) 157–167.
- [31] S. Carrettin, Y. Hao, V. Aguilar-Guerrero, B.C. Gates, S. Trasobares, J.J. Calvino, A. Corma, *Chem. Eur. J.* 13 (2007) 7771–7779.
- [32] A. Penkova, K. Chakarova, O.H. Laguna, K. Hadjiivanov, F. Romero Sarria, M.A. Centeno, J.A. Odriozola, *Catal. Commun.* 10 (2009) 1196–1202.
- [33] O.H. Laguna, M.A. Centeno, G. Arzamendi, L.M. Gandia, F. Romero Sarria, J.A. Odriozola, *Catal. Today* 157 (2010) 155–159.
- [34] O.H. Laguna, F. Romero Sarria, M.A. Centeno, J.A. Odriozola, *J. Catal.* 276 (2010) 360–370.
- [35] S. Albonetti, R. Bonelli, J. Epoupa Mengou, C. Femoni, C. Tiozzo, S. Zacchini, F. Trifirò, *Catal. Today* 137 (2008) 483–488.

- [36] S. Albonetti, R. Bonelli, R. Delaigle, C. Femoni, E.M. Gaigneaux, V. Morandi, L. Ortolani, C. Tiozzo, S. Zacchini, *Appl. Catal. A: Gen.* 372 (2010) 138–146.
- [37] R. Bonelli, S. Albonetti, V. Morandi, L. Ortolani, P.M. Riccobene, S. Scirè, S. Zacchini, *Appl. Catal. A: Gen.* 395 (2011) 10–18.
- [38] D.Y. Zhao, Q.S. Huo, J.L. Feng, B.F. Chmelka, G.D. Stucky, *J. Am. Chem. Soc.* 120 (1998) 6024–6036.
- [39] K. Farmery, M. Kilner, R. Greatrex, N.N. Greenwood, *J. Chem. Soc. A* (1969) 2339–2345.
- [40] V.G. Albano, R. Aureli, M.C. Iapalucci, F. Laschi, G. Longoni, M. Monari, P. Zanello, *J. Chem. Soc., Chem. Commun.* (1993) 1501–1502.
- [41] S. Brunauer, P.H. Emmett, E. Teller, *J. Am. Chem. Soc.* 60 (1938) 309–319.
- [42] E.P. Barrett, L.G. Joyner, P.J. Halenda, *J. Am. Chem. Soc.* 73 (1951) 373–380.
- [43] H.P. Klug, L.E. Alexander, *X-ray Diffraction Procedures for Polycrystalline and Amorphous Materials*, Wiley, New York, 1954.
- [44] JCPDS, *Journal Powder Diffraction File*, Int. Centre for Diffraction Data, Swarthmore, 2010.
- [45] D. Zhao, J. Feng, Q. Huo, N. Melosh, G.H. Fredrickson, B.F. Chmelka, G.D. Stucky, *Science* 279 (1998) 548–552.
- [46] I. Yuranov, P. Moeckli, E. Suvorova, P. Buffat, L. Kiwi-Minsker, A. Renken, *J. Mol. Catal. A: Chem.* 192 (2003) 239–251.
- [47] F. Yin, S. Ji, P. Wu, F. Zhao, C. Li, *J. Catal.* 257 (2008) 108–116.
- [48] K.S.W. Sing, D.H. Everett, R.A.W. Haul, L. Moscou, R.A. Pierotti, J. Rouquerol, T. Siemieniewska, *Pure Appl. Chem.* 57 (1985) 603–619.
- [49] M. Thommes, *Chem. Ing. Tech.* 82 (2010) 1059–1073.
- [50] S. Rada, A. Dehelean, M. Stan, R. Chelcea, E. Culea, *J. Alloys Compd.* 509 (2011) 147–151.
- [51] S.L. Logunov, T.S. Ahmadi, M.A. El-Sayed, J.T. Khoury, R.L. Whetten, *J. Phys. Chem. B* 101 (1997) 3713–3719.
- [52] U. Kreibitz, L. Genzel, *Surf. Sci.* 156 (1985) 678–700.
- [53] J. Pérez-Ramírez, F. Kapteijn, A. Brückner, *J. Catal.* 218 (2003) 234–238.
- [54] M. Høj, M.J. Beier, J.-D. Grunwaldt, S. Dahl, *Appl. Catal. B: Environ.* 93 (2009) 166–176.
- [55] P. Claus, A. Brückner, C. Mohr, H. Hofmeister, *J. Am. Chem. Soc.* 122 (2000) 11430–11439.
- [56] K.M. Parida, et al., *J. Mol. Catal. A: Chem.* 319 (2010) 92–97.
- [57] W.K. Jozwiak, E. Kaczmarek, T.P. Maniecki, W. Ignaczak, W. Maniukiewicz, *Appl. Catal. A* 326 (2007) 17–27.
- [58] G. Neri, A.M. Visco, S. Galvagno, A. Donato, M. Panzalorto, *Thermochim. Acta* 329 (1999) 39–46.
- [59] G. Munteanu, L. Ilieva, D. Andreeva, *Thermochim. Acta* 291 (1997) 171–177.
- [60] C.-W. Chiang, A. Wang, B.-Z. Wan, C.-Y. Mou, *J. Phys. Chem. B* 109 (2005) 18042–18047.
- [61] C.-W. Chiang, A. Wang, C.-Y. Mou, *Catal. Today* 117 (2006) 220–227.